Seasonal and Year-To-Year Variability of Boundary Currents and Eddy Salt Flux along the Eastern and Southern Coasts of Sri Lanka Observed by PIES and Satellite Measurements

A. ANUTALIYA,[a,b] U. SEND,[a] J. L. MCCLEAN,[a] J. SPRINTALL,[a] M. LANKHORST,[a] C. M. LEE,[c] L. RAINVILLE,[c] W. N. C. PRIYADARSHANI,[d] AND S. U. P. JINADASA[e]

[a] *Scripps Institution of Oceanography, La Jolla, California*
[b] *Institute of Marine Science, Burapha University, Chonburi, Thailand*
[c] *Applied Physics Laboratory, University of Washington, Seattle, Washington*
[d] *National Aquatic Resources Research and Development Agency, Colombo, Sri Lanka*
[e] *Ocean University of Sri Lanka, Colombo, Sri Lanka*

(Manuscript received 23 January 2022, in final form 11 July 2022)

ABSTRACT: Boundary currents along the Sri Lankan eastern and southern coasts serve as a pathway for salt exchange between the Bay of Bengal and the Arabian Sea basins in the northern Indian Ocean, which are characterized by their contrasting salinities. Measurements from two pairs of pressure-sensing inverted echo sounders (PIES) deployed along the Sri Lankan eastern and southern coasts as well as satellite measurements are used to understand the variability of these boundary currents and the associated salt transport. The volume transport in the surface (0–200-m depth) layer exhibits a seasonal cycle associated with the monsoonal wind reversal and interannual variability associated with the Indian Ocean dipole (IOD). In this layer, the boundary currents transport low-salinity water out of the Bay of Bengal during the northeast monsoon and transport high-salinity water into the Bay of Bengal during the fall monsoon transition of some years (e.g., 2015 and 2018). The Bay of Bengal salt input increases during the 2016 negative IOD as the eastward flow of high-salinity water during the fall monsoon transition intensifies, whereas the effect of the 2015/16 El Niño on the Bay of Bengal salt input is still unclear. The time-mean eddy salt flux over the upper 200 m estimated for the April 2015–March 2019 period along the eastern coast accounts for 9% of the salt budget required to balance an estimated 0.13 Sv (1 Sv $\equiv 10^6$ m^3 s^{-1}) of annual freshwater input into the Bay of Bengal. The time-mean eddy salt flux over the upper 200 m estimated for the December 2015–November 2019 period along the southern coast accounts for 27% of that same salt budget.

SIGNIFICANCE STATEMENT: In the northern Indian Ocean, the highly saline Arabian Sea undergoes extreme evaporation while the Bay of Bengal (BoB) receives excess freshwater input. The focus of this study is the role of the observed time-variable circulation around Sri Lanka that permits the exchange between these basins to maintain their salinity distributions. The circulation fluctuates seasonally following the monsoon wind reversal and interannually in response to large-scale climate modes. The BoB freshwater export around Sri Lanka occurs during the northeast monsoon, whereas saline water import occurs during the fall monsoon transition of some years. However, rapid changes in both water volume transport and salt exchange can occur. The circulation over 0–200-m depth transports ~9%–27% of the BoB salt budget.

KEYWORDS: Thermohaline circulation; Boundary currents; ENSO; Mass fluxes/transport; Transport

1. Introduction

The Bay of Bengal (BoB), a semienclosed ocean basin in the northeastern Indian Ocean (IO), gains ~0.13 Sv (1 Sv $\equiv 10^6$ m^3 s^{-1}) of freshwater annually from precipitation and river runoff minus evaporation as estimated from observations, reanalysis products, and numerical simulations (Rao and Sivakumar 2003; Sengupta et al. 2006; Wilson and Riser 2016). The large freshwater input into the BoB often creates a barrier layer that occurs between a haline-controlled pycnocline and a deeper thermocline, promoting decoupling between the surface and deeper layer beneath (e.g., Sprintall and Tomczak 1992; Vinayachandran et al. 2002; Thadathil et al. 2007; Girishkumar et al. 2011). The shallow barrier layer results in a highly responsive SST that is found to directly affect rain events during the monsoon (Krishnamohan et al. 2019;

Corresponding author: Arachaporn Anutaliya, arachaporn.an@go.buu.ac.th

DOI: 10.1175/JPO-D-22-0030.1

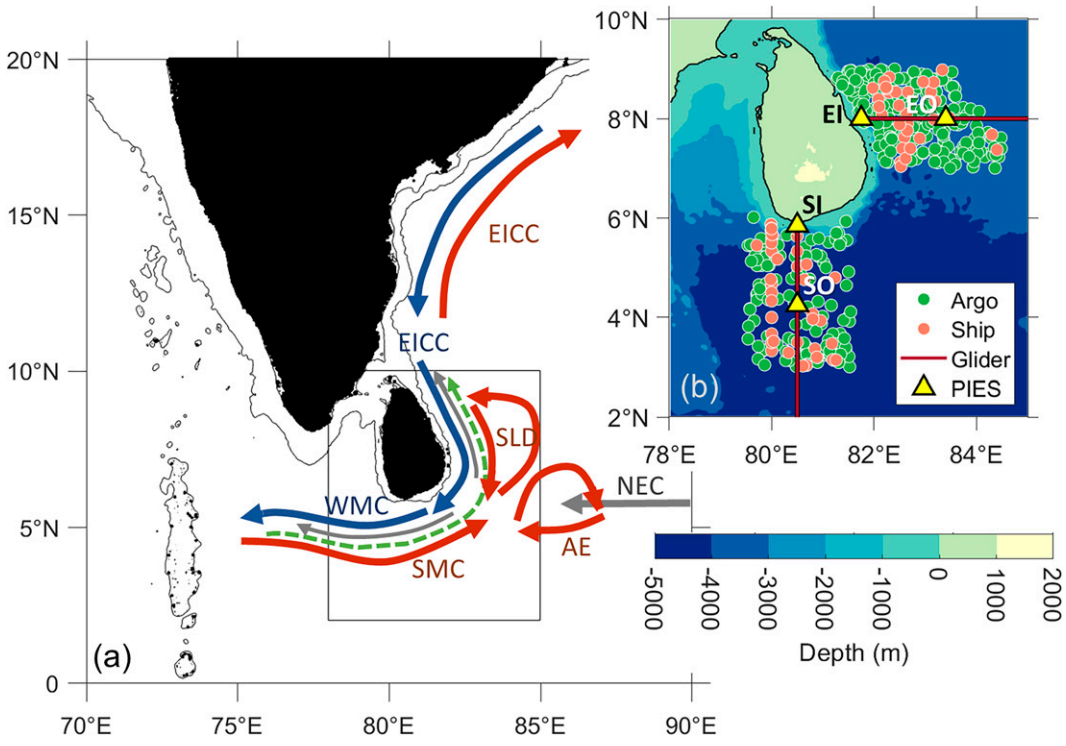

FIG. 1. (a) Map of the observing area and the dominant currents during the southwest monsoon (red), northeast monsoon (blue), spring monsoon transition (gray), and fall monsoon transition during some years (e.g., 2015 and 2018; green dashed). Black contour lines are the 1000-m isobaths. EICC is the East Indian Coastal Current, WMC is the Winter Monsoon Current, SMC is the Summer Monsoon Current, SLD is the Sri Lanka Dome, AE is the seasonal anticyclonic eddy, and NEC is the North Equatorial Current. (b) The inset shows the bathymetry of the Indian Ocean around Sri Lanka with the location of the historical shipboard (orange) and Argo (green) hydrographic profiles, nominal glider tracks (maroon lines), and PIES instruments (yellow triangles) where EI, EO, SI, SO denote different PIES sites: EI eastern inshore; EO eastern offshore; SI southern inshore; SO southern offshore.

Weller et al. 2016) as the warmer SST encourages deep atmospheric convection, particularly during the summer monsoon (Shenoi et al. 2002). In addition, using the wind–evaporation–SST feedback (Xie and Philander 1994) the subsequent rainfall location over the BoB can be predicted when the location of warm SST is identified. Thus, understanding the intensity and fluctuation of the surface salinity layer in the BoB could improve our understanding of the ocean–atmosphere coupling that promotes convection associated with monsoon rainfalls in the northern IO.

One pathway of freshwater export from the BoB is via the seasonal East India Coastal Current (EICC) that occurs during the northeast monsoon (Fig. 1). The EICC extends southward from the eastern coast of India to the eastern coast of Sri Lanka (Shetye et al. 1996). The current then turns westward to merge with the Winter Monsoon Current (WMC; approximately November–February) (Schott et al. 1994; Hacker et al. 1998; Reppin et al. 1999; Rao et al. 2008) that flows along the southern coast of Sri Lanka transporting low-salinity water out of the BoB (Han and McCreary 2001; Wijesekera et al. 2015). The WMC exhibits a similar structure to the EICC in that it intensifies near the coast and in the upper 100–200 m of the water column, although it can extend to 1000-m depth (Schott et al. 1994; Schott and McCreary 2001).

During the southwest monsoon, the eastward Summer Monsoon Current (SMC) transports high-salinity water originating in the Arabian Sea (AS) into the BoB at ~85.5°E (Han and McCreary 2001; Vinayachandran et al. 2013; Wijesekera et al. 2016a; Sanchez-Franks et al. 2019). A seasonal anticyclonic eddy trapping upwelled water off the southern coast of India and Sri Lanka is present to the east of the SMC (Pirro et al. 2020). Along the Sri Lankan eastern coast, the Sri Lanka Dome (SLD), a seasonal cyclonic eddy, dominates the regional circulation (Vinayachandran and Yamagata 1997; Vinayachandran et al. 1999; Shankar et al. 2002; de Vos et al. 2014). Numerical simulations by Jensen (2001) show the intrusion of the AS-originated water into the BoB at the end of the southwest monsoon; Jensen (2003) attributed this to northward Ekman transport arising from the monsoon wind reversal. Analyses using multiple numerical simulations and reanalysis products show that the depth-integrated salt transport across 6°N into the BoB reaches its maximum in July at ~84°E, whereas the maximum salt transport out of the BoB across the same transect reaches its maximum in January at ~82°E (D'Addezio et al. 2015).

Although the WMC and SMC are still found along the southern coast of Sri Lanka during the spring and fall monsoon transitions, respectively (Schott et al. 1994; Schott and McCreary 2001),

the altimetry-derived surface geostrophic flow is northward during both monsoon transitions (Eigenheer and Quadfasel 2000; Durand et al. 2009; Lee et al. 2016). In addition, a seasonal opposing undercurrent below the surface layer is present in boreal spring along the eastern coast (Anutaliya et al. 2017). To date, there have been few continuous or simultaneous measurements of flows off the Sri Lankan eastern and southern coasts to demonstrate the regional circulation and its contribution to BoB freshwater export.

In this study, we use continuous measurements from nearly simultaneous 4-yr deployments of seafloor pressure-sensing inverted echo sounders (PIES) from 2014 to 2019 off the Sri Lankan eastern and southern coasts and surface velocity from satellite altimetry to estimate the volume transport within these boundary currents and understand the regional circulation. Together with remotely sensed sea surface salinity (SSS), we use the PIES measurements to estimate eddy salt fluxes along the Sri Lankan eastern and southern coasts. In addition to the seasonal monsoon, we also examine the impact on this circulation from interannual climate modes, such as the Indian Ocean dipole (IOD) and El Niño–Southern Oscillation (ENSO). The datasets and method are described in sections 2 and 3, respectively. Section 4 presents the observed velocity, volume transport, and eddy salt flux across the Sri Lankan eastern and southern sections. Section 5 contains the summary.

2. Datasets

a. In situ measurements

The PIES were deployed on the seafloor to measure bottom pressure and acoustic travel time. The bottom pressure fluctuation captures the barotropic flow fluctuation while the acoustic travel time reflects baroclinic flow, mainly contributed by temperature variations in the water column plus the effect of sea surface height changes (e.g., Meinen and Watts 2000; Lee et al. 2016). As suggested by altimeter data and also Seaglider measurements (Rainville et al. 2022), the boundary currents extend from the coasts to approximately 170 km offshore, although the location and width of the flow along the southern coast varies seasonally (Schott et al. 1994). A pair of PIES were deployed off the eastern coast [8.00°N, 81.75°E: site EI (eastern inshore) and 8.00°N, 83.40°E: site EO (eastern offshore)] and off the southern coast of Sri Lanka [5.85°N, 80.50°E: site SI (southern inshore) and 4.25°N, 80.50°E: site SO (southern offshore)], spaced ~180 km on each section to bracket the expected position of the boundary currents along each of the Sri Lankan coasts (Fig. 1). The eastern pair were deployed from November 2014 to March 2019, and the southern pair were deployed from December 2015 to November 2019. Both inshore PIES were at ~600-m depth (24 km off the eastern coast and 8 km off the southern coast), and both offshore PIES were at ~4000-m depth. PIES bottom pressure was processed to eliminate the known exponential-linear instrument drift and tidal signals (Kennelly et al. 2007). The resulting pressure fluctuations resolve variability shorter than the deployment period (~4 years). Acoustic travel time data off the southern coast at the inshore location (SI) are missing because of instrument issues.

A priori in situ measurements of the water column structure are necessary to estimate water transport from the PIES travel time and bottom pressure. Local conductivity–temperature–depth (CTD) profiles from historical shipboard hydrography, autonomous gliders, and Argo floats (Anutaliya et al. 2017) were used to establish a relationship [see section 3a(1)] between the integrals of the baroclinic flow relative to a bottom reference (i.e., the PIES bottom pressure) and a linear combination of PIES acoustic travel time and satellite altimetry. There were 281 profiles (30 profiles from shipboard hydrography and 251 profiles from Argo floats) sampled within the eastern box and 185 profiles (39 profiles from shipboard hydrography and 146 profiles from Argo floats) sampled within the southern box (see inset of Fig. 1). The CTD profiles sampled to depths between 600 and 2000 m. All temperature–salinity profiles were used to simulate the acoustic travel time signal for the inshore PIES (~600-m depth), but only those that sampled to 2000 m (214 profiles off the eastern coast and 136 profiles off the southern coast) were used to simulate the acoustic travel time signal for the offshore PIES (~4000-m depth). The available CTD profiles only sample to 2000-m depth, but the potential temperature and salinity between 2000- and 4000-m depth over the region do not vary much (Shetye et al. 1993; Garternicht and Schott 1997; Beal et al. 2003). Therefore, temperature and salinity were extrapolated from 2000 to 4000 m by assuming that potential temperature and salinity remained constant below 2000 m.

Seagliders were deployed nominally along these same sections as the PIES because they were part of larger observational programs: Air–Sea Interactions Regional Initiative (ASIRI; Wijesekera et al. 2016b) and Monsoon Intra-Seasonal Oscillations in Bay of Bengal (MISO-BoB; Shroyer et al. 2021). The Seagliders repeatedly sampled temperature and salinity from the surface to ~1000-m depth from December 2013 to January 2016 off the Sri Lankan eastern coast and from April 2016 to December 2019 off the southern coast (Lee et al. 2016; Rainville et al. 2022; Fig. 1). Although the glider sections extend farther to the east or south than the offshore PIES locations considered here, there is significant overlap between the PIES and glider sections (by design). Gliders take 1–2 weeks to travel the distance between the PIES. There are 14 crossings, with 6 of the glider crossings overlapping with the PIES observing period, at the eastern section and 36 crossings, with 32 of the glider crossings overlapping with the PIES observing period, at the southern section. In this study, the glider-derived geostrophic velocity and salinity measurements are primarily used to calibrate and validate the time series of volume transport and eddy salt flux as estimated by the PIES and satellite measurements. In addition, the typical vertical structure (modes) calculated from the glider velocity profiles were used to retrieve details of the velocity structure once total transports in the surface and subsurface layers were determined from PIES and satellite altimetry data. In addition, errors associated with the eddy salt flux estimation method based on PIES, satellite altimetry, and SSS at the sections are estimated using simulations of the method with salinity and

velocity measurements from the Seagliders. Water properties and transports estimated from gliders are discussed in detail elsewhere (Rainville et al. 2022).

b. Remotely sensed data

The gridded SLA is available over the 1993–2019 period on a 1/4° grid at daily resolution (Ducet et al. 2000). The satellite SLA measures expansion of the water column due to both temperature and salinity variations plus mass changes. The SLA was linearly interpolated onto the 8.00°N eastern and 80.50°E southern sections (Fig. 1) to combine with the PIES acoustic travel time and estimate baroclinic flow across the sections.

Remotely sensed SSS is derived from Soil Moisture Active Passive V4.0 (SMAP; Meissner et al. 2018). The product is an 8-day running average with 40-km spatial resolution interpolated onto a 1/4° grid and is available from April 2015 to December 2019. The SSS is linearly interpolated onto the 8.00°N eastern and 80.50°E southern sections (Fig. 1) and is used to estimate the eddy salt flux carried by the boundary currents.

3. Method

a. Volume transport calculation

1) Volume transport fluctuation from PIES and satellite altimetry

PIES provide acoustic travel time and bottom pressure measurements. Traditionally, acoustic travel times can be related to the existing historical CTD temperature and salinity profiles of the measured water column to create lookup tables for each variable; the technique is referred to as the gravest empirical mode (GEM) method (Meinen and Watts 2000; Watts et al. 2001). From the lookup tables, the temperature and salinity structure of the water column can be inferred from the measured acoustic travel time. Thus, the baroclinic volume transport can be calculated over the depth layer being investigated. However, the water column structure is highly variable. As a result, the GEM method does not work well in the region.

Instead of parameterizing temperature and salinity profiles, we developed a technique that directly relates the quantity of interest (integral of the geopotential, referenced to the bottom, over the target layer; G') to known quantities, which are the PIES acoustic travel time and the satellite SLA. The quantity G' is combined with the geopotential fluctuation at the reference depth, that is, the bottom, Φ derived from the PIES bottom pressure (i.e., $\Phi = p'/\rho$, where ρ represents mean density at the PIES depth) to obtain the total (absolute) geopotential integral G over the surface or subsurface layer with a thickness of Δz:

$$G = G' + \Phi\Delta z, \tag{1}$$

where Δz is 200 m for the surface layer and 400 m for the subsurface layer. This new technique gives a more robust relationship of the measured quantities with the quantities of interest since G' is a double integral of specific volume anomaly over the desired pressure range. The relationship between G' and a combination of acoustic travel time and satellite SLA is found empirically through multivariable linear regression and it is determined separately for each PIES site. At each PIES site, the PIES acoustic travel time is simulated from the nearby historical hydrography (see inset Fig. 1) adjusted for the height of the water column using collocated (in both space and time) satellite SLA. The height adjustment is required to accurately calculate the travel time integral from the PIES depth to the actual sea surface. Because historical hydrography shows that the boundary current is concentrated in the upper 200 m of the water column (Anutaliya et al. 2017), the integral of geopotential was estimated over the upper 200 m of the water column (surface layer) separately from that over the 200–600-m-depth (subsurface) layer.

To obtain the accuracy of the G' estimates, a scatterplot between the surface-layer G' that is directly computed from historical hydrography (CTD G') and G' that is determined from the empirical relationship based on the travel time and satellite altimetry (model G') at each PIES location is examined (Fig. 2). For the surface layer (sfc), the correlation between CTD G'_{sfc} and model G'_{sfc} is very high (>0.7) at all four locations and is significant at the 95% confidence level. Since the travel time is missing at the SI site, only SLA is used to linearly regress against G'_{sfc}, and this yields the lowest correlation coefficient of 0.74 between CTD G'_{sfc} and model G'_{sfc}. In the 200–600 m subsurface layer (sub), the correlation between CTD G'_{sub} and model G'_{sub} is significant at the 95% confidence level at the EI, EO, and SO sites, with correlation coefficients ranging from 0.75 to 0.83. The correlation at the SI site is only 0.13 and is not significant at the 95% confidence level because the acoustic travel time at this site is missing and altimetry SLA apparently does not constraint the 200–600-m dynamic height. To examine whether bottom pressure alone can constrain the subsurface layer dynamic height, the barotropic component [$\Phi(t)\Delta z$; Eq. (1)] is estimated by calculating bottom pressure from historical CTD measurements adjusted for the surface height using collocated satellite SLA. The result shows that the barotropic contribution from the PIES bottom pressure dominates the subsurface absolute geopotential fluctuation at this site; calculating the absolute geopotential integral fluctuation (both baroclinic and barotropic contributions) using $G'^{\mathrm{In}}_{\mathrm{sub}}$ estimated without the acoustic travel time results in only ~8% root-mean-square (rms) difference from that computed using $G'^{\mathrm{In}}_{\mathrm{sub}}$ estimated using both satellite SLA and acoustic travel time.

From the geopotential estimated separately at the inshore and offshore locations, the temporal fluctuations of the volume transport Q' at each time step t in the surface layer can be calculated as

$$Q'_{\mathrm{sfc}}(t) = \frac{1}{f}[G^{\mathrm{Off}}_{\mathrm{sfc}}(t) - G^{\mathrm{In}}_{\mathrm{sfc}}(t)], \tag{2}$$

where f is the Coriolis parameter at the midsection location (8.00°N for the eastern section and 5.05°N for the southern section). The superscript denotes the location of the inshore

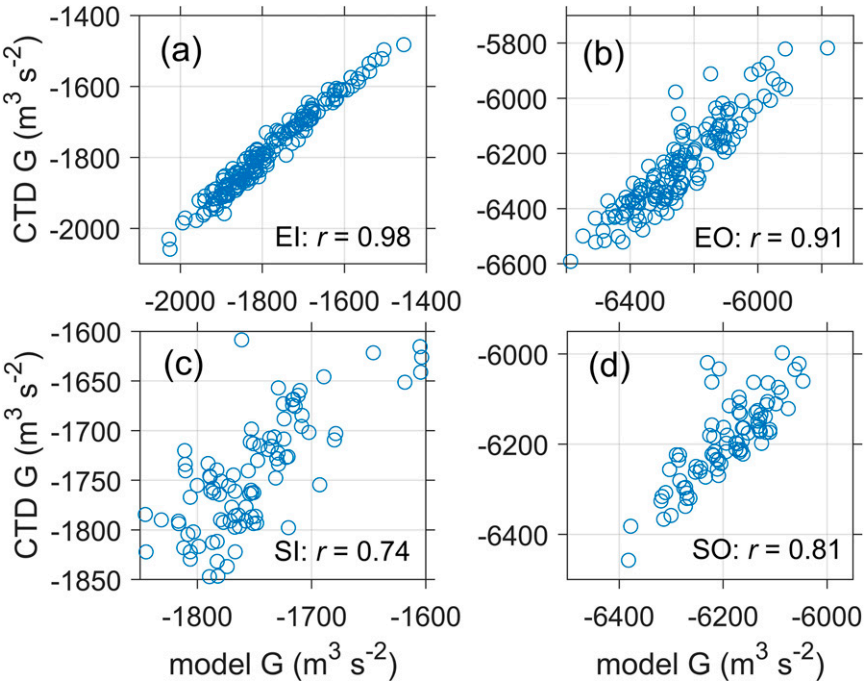

FIG. 2. Scatterplots of the vertical integral of the geopotential G_{sfc} over the 0–200-m layer referenced to the PIES depths calculated from historical CTD profiles (y axis) vs that obtained through a linear regression model against the CTD-simulated acoustic travel time and satellite SLA (x axis) at the (a) EI, (b) EO, and (d) SO sites. Only satellite SLA was used for the model G_{sfc} at the (c) SI site. The corresponding correlation coefficients are shown in the lower-right corners of each subplot. The G_{sfc} is calculated with reference levels at the PIES depths, i.e., 600-m depth for the inshore location and 4000-m depth for the offshore location.

(In) and offshore (Off) PIES. Volume transport fluctuations in the 200–600-m subsurface layer are calculated correspondingly, but by using G_{sub} instead of G_{sfc}.

2) ABSOLUTE VOLUME TRANSPORT AND ACROSS-SECTION MEAN VELOCITY PROFILE CONSTRUCTION

The geostrophic transports obtained with the above approach have an unknown time-mean offset that corresponds to the unknown absolute levelling of the two PIES bracketing each section. To estimate the mean offset, we use volume transport calculated from the Seaglider measurements over the section spanned by the PIES and over the surface (0–200-m depth) and subsurface (200–600-m depth) layers. There are 6 and 32 glider crossings that overlap with the PIES/altimetry volume transport off the eastern and southern coasts, respectively. For each Seaglider transect crossing, the PIES/altimetry-derived volume transport fluctuation Q' is averaged over the time period of the glider crossing, and Q' is computed separately in the surface and subsurface layers. The time-mean adjustment to the PIES transports is the average of the differences between Seaglider absolute volume transport and the PIES/altimetry-derived transport fluctuation over all of the Seaglider crossings. This time-mean offset of −0.3 Sv was added to the PIES/altimetry surface-layer volume transport fluctuation, while that of −2.8 Sv was added to the subsurface-layer fluctuation across the eastern section. In addition, this time-mean offset of −2.2 Sv was added to the PIES/altimetry surface-layer volume transport fluctuation, while that of 0.5 Sv was added to the subsurface-layer fluctuation across the southern section. The adjusted volume transport will be referred to as PIES/altimetry absolute volume transport. Although there is some uncertainty in these offsets because of the small number of overlapping glider crossings, the main focus of this study is on the fluctuating component of the flow, and thus our analysis is not sensitive to the offset choice.

For the salt transports (see section 3b), we need to construct the vertical structure of the across-section mean velocity in the upper water column from our continuous PIES/altimetry volume transport estimates in the surface and subsurface layers. Vertical empirical orthogonal functions (EOFs) from the Seaglider velocity profiles sampled along the PIES section were calculated and used to serve as a priori information about the vertical structure. At each time step, the PIES/altimetry-derived volume transports in the surface and subsurface layer were projected onto the two most dominant EOFs calculated from Seaglider measurements to obtain the velocity profile (Fig. 3; Anutaliya et al. 2019).

3) UNCERTAINTY ASSOCIATED WITH THE CALCULATED VOLUME TRANSPORT

Uncertainties associated with the PIES/altimetry-based volume transport are mainly contributed by two sources:

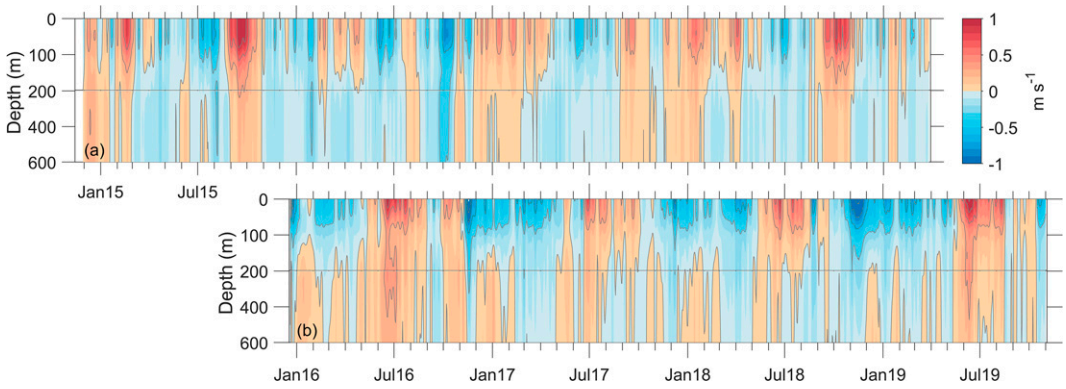

FIG. 3. Across-section mean geostrophic velocity (m s^{-1}) estimated from the PIES/altimetry surface and subsurface volume transport for the (a) eastern and (b) southern sections. Color contour intervals are 0.05 m s^{-1}, and gray contours are plotted every 0.3 m s^{-1}. Note the expanded y axis over the 0–200-m-depth layer.

instrument accuracy and the calculation technique [Eqs. (1) and (2), together with the regression relationships derived from Fig. 2]. At the eastern and southern sections, uncertainty in the surface-layer volume transport of 0.6 and 0.8 Sv, respectively, is associated with the instrument accuracy as the instrument error is ~0.01% of the pressure range. The error associated with the acoustic travel time measurement is included in uncertainty of the calculation technique (Meinen and Watts 1998), which is shown in the scatterplot (Fig. 2); the uncertainty is 3.9 and 6.4 Sv at the eastern and southern sections, respectively. The total uncertainties, calculated as the sum of variances produced by both components, are 4.0 and 6.4 Sv for the surface volume transport across the eastern and southern sections, respectively. The PIES/altimetry surface-layer absolute volume transport at the southern section agrees with the glider transport within the uncertainty (rms difference is 4.5 Sv). At the eastern section, however, the rms difference between the PIES/altimetry and glider surface-layer volume transport is 7.9 Sv, larger than the estimated uncertainty, which is likely a consequence of fewer overlapping measurements by the PIES and the glider [section 3a(2) above]. For the subsurface layer, the uncertainty for the flow along the eastern coast is 7.1 Sv, of which 7.0 Sv is from the calculation technique and 1.2 Sv is from the instrument accuracy, and the uncertainty for the flow along the southern coast is 10.0 Sv, of which 9.9 Sv is from the calculation technique and 1.6 Sv is from the instrument accuracy. The uncertainty due to the calculation technique is very high for the subsurface flow along the southern coast because the acoustic travel time measurement at the SI site is missing; hence, the subsurface G' cannot be accurately estimated, as noted above.

b. *Eddy salt transport estimation*

The eddy salt flux component is then determined as the product of the temporal fluctuations of salinity $[\tilde{S}(s,z,t)]$ and velocity $[\tilde{v}(s,z,t)]$ at each section, where a tilde denotes the temporal fluctuation relative to the mean vertical profile $\overline{x}(z)$ [the overbar denotes averages over the section (section mean) and over the observing period (time mean) of a quantity x]; that is, $\tilde{x}(s,z,t) = x(s,z,t) - \overline{x}(z)$. The time series will be hereinafter referred to as the eddy salt *transport* $F_s(t)$, and the time-mean of the eddy salt transport is the eddy salt *flux* $\overline{F}_s$. The eddy salt transport is calculated as follows:

$$F_s(t) = \int_{z=0}^{200}\int_{s^{\mathrm{In}}}^{s^{\mathrm{Off}}} \overline{\rho}(z)\tilde{S}(s,z,t)\tilde{v}(s,z,t)\, ds\, dz, \qquad (3)$$

where s^{In} and s^{Off} represent the location of PIES at the inshore and offshore sites, respectively, and $\overline{\rho}(z)$ is the time-mean density that is determined from the historical hydrography averaged over each section. The $\overline{v}(z)$ is derived from the reconstruction based on the PIES/altimetry volume transport and Seaglider EOFs [section 3a(2); Fig. 3], and $\overline{S}(z)$ is from the local hydrography. At the surface, the SMAP mean SSS is 33.4 and the mean SSS from local hydrography is 33.8 at the eastern section whereas the SMAP mean SSS is 34.1 and the mean SSS from local hydrography is 34.5 at the southern section. The different time-mean SSS from the hydrography and from the satellite SSS is likely a result of the combination of the different sampling periods, the extrapolation of the hydrographic salinity profile to the surface, and potential biases in the satellite product (Tang et al. 2017; Qin et al. 2020). Therefore, the hydrography-derived $\overline{S}(z)$ used for the eddy salt flux estimation is scaled and shifted (linearly transformed); constants for shifting and scaling are determined so that $\overline{S}(z)$ passes through the satellite time-mean SSS while salinity at 600-m depth remains the same. From Eq. (3), $\tilde{S}(s,z,t)$ and $\tilde{v}(s,z,t)$ are needed but cannot be directly obtained from either the PIES measurements or satellite SMAP SSS. Thus, these quantities have to be inferred from available information as described in the following sections.

1) SALINITY PROFILE CONSTRUCTION

To calculate eddy salt transport, a salinity profile at locations along the section at each time step $[S(s, z, t)]$ is required; however, satellite measurements can only provide the time series of salinity at the surface along the section $[S(s, 0, t)]$. Therefore, we used the local historical CTD measurements to estimate the salinity structure below the surface at each time along each section based on either altimetry-derived surface

velocity or SMAP SSS. The details of the salinity profile construction can be found in the appendix.

Because there is no continuous measurement of 200–600 m salinity available for the salinity profile construction, we are not confident of the estimated salinity over the deeper subsurface layer. Therefore, eddy salt transport will only be calculated for the upper 200 m of the water column. Also, both observations and numerical simulations show that the eddy salt flux below 200 m is likely small (Anutaliya et al. 2017; Rainville et al. 2022).

2) VELOCITY PROFILE CONSTRUCTION

While the time series of velocity profiles (PIES/altimetry volume transport with Seaglider EOFs) were constructed as along-section means [section 3a(2); Fig. 3], the velocity profile at locations *along* each section [$v(s, z, t)$] is needed for the eddy salt transport estimation [Eq. (3)]. This quantity is estimated by projecting the altimetry-derived surface velocity at each section onto the two leading modes of the Seaglider EOFs, constrained by the total across-section transports in the surface (0–200 m) and subsurface (200–600 m) layers from the PIES. Among the possible solutions, the one with the smallest rms velocity in the subsurface layer is chosen, which we found to give results resembling the actual flow distributions.

3) SECTION-MEAN AND SECTION-VARYING COMPONENTS OF EDDY SALT TRANSPORT

The $F_s(t)$ can be decomposed into two components: the first component results from the section-mean salinity fluctuation, $S^*(z, t)$ defined as $\langle \tilde{S}(s,z,t) \rangle$, and velocity fluctuation, $v^*(z, t)$ defined as $\langle \tilde{v}(s,z,t) \rangle$, where the angle brackets indicate the section-mean, and the second component is the departure from the section-mean (spatially fluctuating) parts [e.g., $S'(s, z, t)$]. By decomposing $\tilde{S}(s,z,t)$ and $\tilde{v}(s,z,t)$ into the section-mean and spatially fluctuating part, Eq. (3) can be rewritten as follows:

$$F_s(t) = \int_{z=0}^{200} \int_{s^{\mathrm{In}}}^{s^{\mathrm{Off}}} \overline{\rho}(z) S^*(z,t) v^*(z,t) + \overline{\rho}(z) S'(s,z,t) v'(s,z,t)\, ds\, dz. \quad (4)$$

We can compute the first component of Eq. (4) from the time-varying section-mean velocity (i.e., Fig. 3) and the section-mean salinity profile constructed from the section-mean SMAP SSS and the local hydrography (see the appendix). In situ measurements of salinity and velocity profiles from the Seaglider can be used to evaluate the percentage of variance in eddy salt transport captured by the calculation using only the section means, that is, the first term in Eq. (4). In addition, Seaglider measurements allow the estimation of uncertainties associated with the eddy salt transport calculation using solely the first (section mean) component as compared with the total eddy salt transport (section-mean and spatially fluctuating components). Thus, we can determine the appropriate technique for the eddy salt transport calculation at each section. Simulations with the Seaglider measurements show that the section-mean eddy salt transport alone [first component; calculated on the basis of $S^*(z, t)$ and $v^*(z, t)$] accounts for 62% of the total eddy salt transport variability at the eastern section. At the southern section, the section-mean eddy salt transport accounts for 83% of the total eddy salt transport variance. The uncertainties in eddy salt flux are 0.20×10^6 and 0.16×10^6 kg s^{-1} at the eastern and southern section, respectively (Table 1). Thus, the eddy salt flux component derived from $S^*(z, t)$ and $v^*(z, t)$ alone approximately represents the total eddy salt flux for the sections, particularly off the southern coast.

TABLE 1. Uncertainties associated with time series mean and annual mean (in parentheses) salt flux estimation ($\times 10^6$ kg s^{-1}) using section-mean and section-depth velocity v and salinity S at the eastern and southern sections. The estimated mean salt flux values ($\times 10^6$ kg s^{-1}) at the eastern section are based on the section-depth v and S, whereas the mean salt flux values ($\times 10^6$ kg s^{-1}) at the southern section are based on the section-mean v and S [$\langle v(s, z, t) \rangle$ and $\langle S(s, z, t) \rangle$].

	Uncertainty ($\times 10^6$ kg s^{-1})		
	$\langle v(s, z, t) \rangle$ and $\langle S(s, z, t) \rangle$	Section-depth v and S	Estimated time series mean salt flux ($\times 10^6$ kg s^{-1})
East	0.20 (0.39)	0.08 (0.17)	0.42
South	0.16 (0.31)	0.21 (0.42)	1.29

For a more accurate estimate of the total eddy salt transport [Eq. (4)], both section-mean [$S^*(z, t)$ and $v^*(z, t)$] and spatially varying salinity and velocity profiles [$S'(s, z, t)$ and $v'(s, z, t)$] are required. Each PIES section is divided into four equally spaced (~45 km) grid cells beginning at the coast (81.75°E for the eastern and 5.75°N for the southern section). To obtain the along-section/depth distribution of salinity, SMAP SSS is linearly interpolated to the center of each grid cell where subsurface salinity structure is separately determined based on the historical hydrography (see the appendix). The along-section/depth distribution of velocity is estimated according to section 3b(2), where surface velocity calculated from satellite altimetry is also linearly interpolated to the center of each grid cell. Again, the Seaglider measurements were used to simulate the additional variance of the eddy salt transport captured by including both section-mean and spatially fluctuating components in the calculation. Then, we compare the resulting eddy salt transport from the simulated sections with that calculated from the full Seaglider salinity and velocity profiles. At the eastern section, the eddy salt transport calculated from the section–depth salinity/velocity [both $S^*(z, t)$, $v^*(z, t)$ and $S'(s, z, t)$, $v'(s, z, t)$] explains a higher percentage of variance (88%) of the eddy salt transport. The uncertainty in eddy salt flux also decreases to 0.08×10^6 kg s^{-1} (Table 1). However, on the southern section the Seaglider measurements show that both $S^*(z, t)$, $v^*(z, t)$ and $S'(s, z, t)$, $v'(s, z, t)$ together only explain 53% of the total eddy salt transport variance, decreasing the skill in estimating the eddy salt transport in comparison with the section-mean salinity/velocity. Also, the uncertainty in eddy salt flux estimation increases to 0.21×10^6 kg s^{-1} (Table 1). The higher uncertainty at the southern section reflects the inability of the constructed along-section/depth distributions of salinity/velocity to adequately replicate the vertical structure of the salinity and velocity along the section. Indeed, the glider

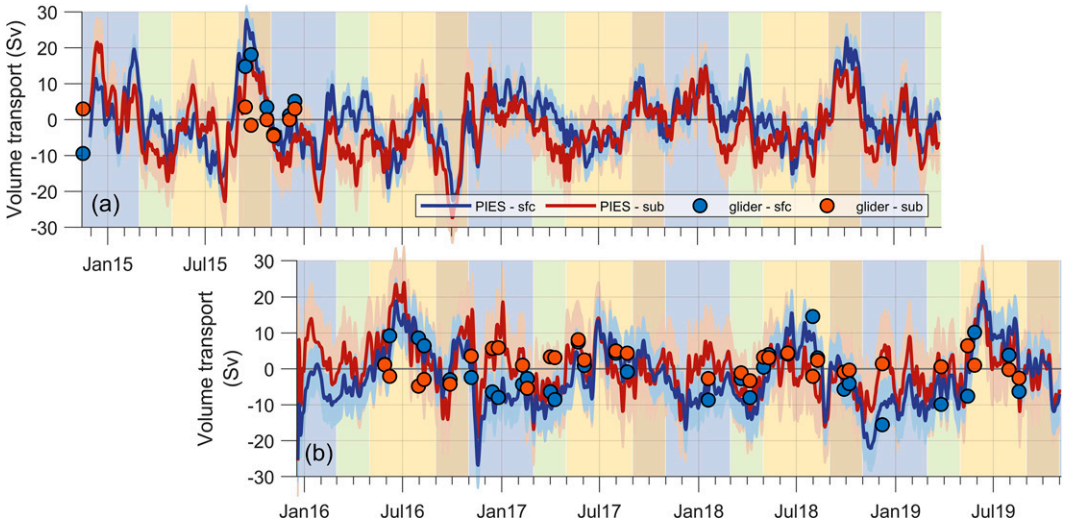

FIG. 4. Volume transport (Sv) across the section off the Sri Lankan (a) eastern and (b) southern coasts over the 0–200-m-depth (surface; blue) and 200–600-m-depth (subsurface; red) layers. Results from the PIES measurements and satellite SLA are shown as lines, with the associated uncertainties shaded. Results from the Seaglider measurements are shown as dots. Background shading denotes the seasons of northeast monsoon (blue), spring monsoon transition (green), southwest monsoon (yellow), and fall monsoon transition (brown).

measurements along the southern section show that the salinity and velocity in the upper 200 m of the water column are complex; a subsurface salinity maximum is sometimes present between 40- and 120-m depth, while the velocity section often shows subsurface reversing flow (Rainville et al. 2022). Therefore, $F_s(t)$ across the eastern section is determined from both components in Eq. (4) [$S^*(z,t)$, $v^*(z,t)$ and $S'(s,z,t)$, $v'(s,z,t)$], whereas that across the southern section is determined from the section [only the first component in Eq. (4): $S^*(z,t)$ and $v^*(z,t)$].

4. Results and discussion

a. *Overall description of the circulation along Sri Lankan eastern and southern coasts*

The volume transports along the eastern and southern coasts of Sri Lanka have similar mean values and ranges in both the surface (0–200-m depth) and subsurface (200–600-m depth) layers. In the surface layer, volume transport along the eastern coast ranges from −22.6 to 27.8 Sv with a mean of −0.1 Sv over the whole observing period of November 2014–March 2019 and volume transport along the southern coast ranges from −26.8 to 24.2 Sv with a mean of −0.2 Sv over the whole observing period of December 2015–November 2019 (Fig. 4). A positive sign designates northward flow along the eastern coast and eastward flow along the southern coast. The mean surface-layer volume transport along the eastern coast over the full 4-yr period from the beginning of 2015 to the end of 2018 is −0.2 Sv. Along the southern coast, the PIES observations do not cover the whole 4-yr period; data from most of November and the first half of December, when the flow is seasonally westward, are missing. Thus, we expect the full 4-yr mean to be lower than −0.2 Sv (i.e., stronger westward). The estimated mean volume transport along the southern coast is roughly consistent with previous mooring transport observations where the volume transport is not significantly different from 0 over a 3.75°–5.87°N section in the 0–300-m-depth layer (Schott et al. 1994). In the subsurface layer, the mean volume transport along the eastern coast is −2.7 Sv, ranging from −27.3 to 21.5 Sv, and the mean volume transport along the southern coast is 0.5 Sv, ranging from −25.6 24.2 Sv. At the eastern section, the 2015–18 mean subsurface volume transport is −3.0 Sv (Fig. 4). Along both coasts, the volume transports in the surface and subsurface layers are correlated with correlation coefficient of 0.74 and 0.68 at the eastern and southern sections, respectively; the correlations are significant at the 95% confidence level.

Along the Sri Lankan eastern coast, the geostrophic velocity time series confirm the *surface* circulation variability found by previous observational studies (e.g., Hacker et al. 1998; Shankar et al. 2002; de Vos et al. 2014; Wijesekera et al. 2015; Lee et al. 2016); the surface current reverses its direction twice a year flowing southward during the monsoon seasons and northward during transition periods (Figs. 3a and 4a). The PIES-altimetry volume transport also shows a subsurface current that occasionally flows in the opposite direction to the surface current (Fig. 3a). The timing of these appearances generally corresponds to previously identified periods during the spring monsoon transition and southwest monsoon when a subsurface countercurrent is present (Anutaliya et al. 2017). Along the Sri Lankan southern coast, the velocity derived from the PIES-altimetry observations exhibits a strong seasonal cycle in the surface layer consistent with observations of the surface current based from satellite altimetry and moorings (Fig. 5; Eigenheer and Quadfasel 2000; Durand et al. 2009; Schott et al. 1994). The dominant surface current along

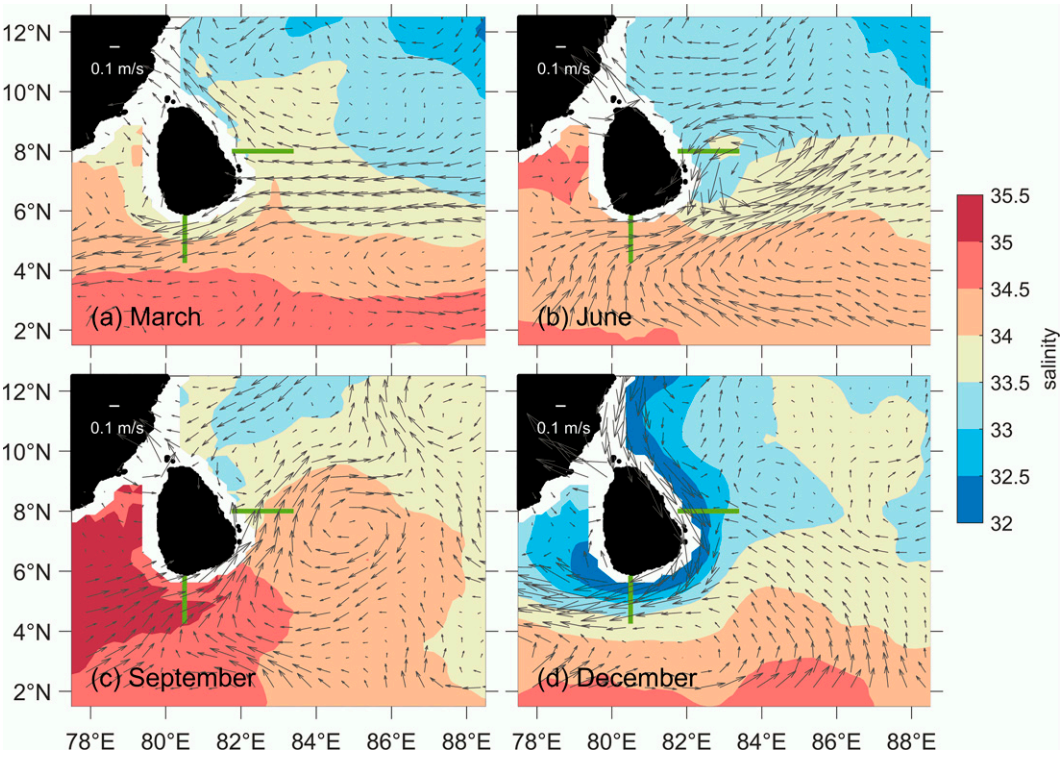

FIG. 5. Monthly mean SMAP sea surface salinity for April 2015–December 2019 (color contours) and geostrophic sea surface velocity derived from satellite altimetry (gray arrows) for the months representing (a) the spring monsoon transition corresponding to green shading in Figs. 4 and 6 (March), (b) the southwest monsoon corresponding to yellow shading in Figs. 4 and 6 (June), (c) the fall monsoon transition corresponding to brown shading in Figs. 4 and 6 (September), and (d) the northeast monsoon corresponding to blue shading in Figs. 4 and 6 (December).

the southern coast is eastward in June–October and westward in November–May; however, the subsurface flow does not show a distinct seasonal cycle. The PIES and altimetry provide the first set of nearly simultaneously observations along the Sri Lankan eastern and southern coasts that continuously capture the regional circulation as well as the eddy salt transport, which will be described in the next sections (sections 4b–d).

b. *Overall eddy salt transport by the boundary currents*

The estimated salt transport [F_s (t)] across the eastern section in the upper 200 m of the water column has a mean of 0.42×10^6 kg s^{-1} over the April 2015–December 2018 period (when the SMAP SSS is available). At the Sri Lankan southern coast, the salt transport is mainly positive over the observing period (Fig. 6b) yielding the mean eddy salt flux of 1.29×10^6 kg s^{-1} over the period of December 2015–November 2019 (Table 1). A positive time-mean eddy salt flux indicates that either fresher water is being transported southward or more saline water is being transported northward along the Sri Lankan eastern coast and either fresher water is being transported westward or more saline water is being transported eastward along the Sri Lankan southern coast; both conditions result in an increase of the salinity in the BoB. Note that the estimated eddy salt transport is missing from 19 June 2019 to 23 July 2019 because of an interruption of the SMAP instrumentation sampling. The estimated salt transport [F_s (t)] based on PIES, satellite altimetry, and SMAP SSS exhibits high seasonal and year-to-year variability and agrees with that estimated from Seaglider measurements at both sections when they overlap (Fig. 6). Any inconsistency is likely a consequence of the subsurface salinity profile that shows large variability and so cannot always be successfully replicated through our simple construction (see the appendix).

Previous estimates, from climatology, reanalysis products, and numerical simulations, give an overall long-term freshwater input into the BoB of ~0.13 Sv annually (Rao and Sivakumar 2003; Sengupta et al. 2006; Wilson and Riser 2016), which translates into ~4.5×10^6 kg s^{-1} of salt input to maintain the salinity balance in the BoB. Our measurements show that the mean eddy salt flux along the eastern coast of Sri Lanka contributes approximately 9% while that along the southern coast contributes about 27% to the estimated BoB annual salt budget (Table 1). The year-to-year changes in the boundary current eddy salt flux can be 12%–28% of the BoB total salt budget (Table 2). Also, the eddy salt transport is highly variable on the seasonal time scale (Fig. 6).

The seasonal cycle in $F_s(t)$, constructed as the sum of the annual and semiannual harmonics, explains 21% and 23% of the total variance at that the eastern and southern sections,

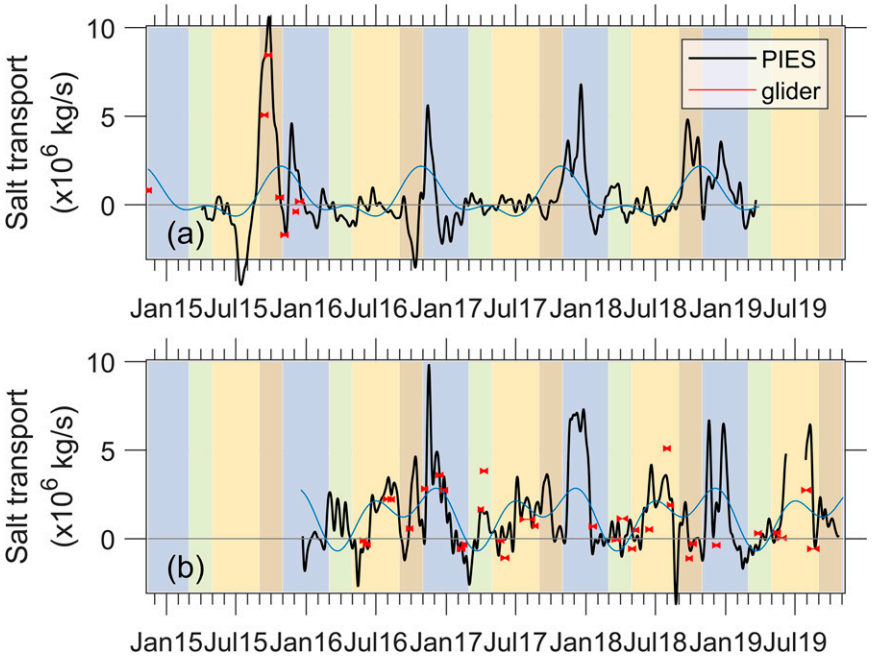

FIG. 6. Estimated eddy salt flux across the Sri Lankan (a) eastern and (b) southern sections. Values in (a) are computed from section-depth velocity and salinity, whereas values in (b) are computed from section-mean velocity and salinity. Glider results are shown in red, and results from PIES, satellite altimetry, and SMAP SSS are shown in black. The lengths of the red symbols represent the time it took the glider to complete the crossing bracketed by the PIES. The seasonal cycles, constructed as the sums of the annual and semiannual harmonics, are plotted in blue. Background shading denotes monsoon seasons as in Fig. 4.

respectively (Fig. 6). The seasonal cycle of eddy salt flux off the Sri Lankan eastern coast exhibits a maximum in October and minimum negative salt transport at the end of June. Off the southern coast, the seasonal cycle is roughly equally influenced by the annual and semiannual harmonics and consists of a maximum seasonal eddy salt flux at the beginning of December with a secondary lower maximum at the beginning of July and a minimum in March. The low-frequency (>120 days) component of $F_s(t)$ explains 15% of the total eddy salt transport variability at the eastern section, whereas it explains 4% of the total variability at the southern section.

TABLE 2. Annual-mean eddy salt flux ($\times 10^6$ kg s^{-1}) computed from the section-depth velocity and salinity at the eastern section and from the section-mean velocity $[\langle v(s, z, t)\rangle]$ and salinity $[\langle S(s, z, t)\rangle]$ at the southern section. Note that the average value along the eastern coast in 2015 only includes the eddy salt transport from April to December and that the average value along the southern coast in 2019 only includes the transport from January to November.

	East	South
2015	1.05	—
2016	−0.23	1.51
2017	0.47	1.48
2018	0.62	1.17
2019	—	0.98

c. *Seasonal variability of the regional circulation*

1) SOUTHWEST MONSOON (MAY–AUGUST)

Off the Sri Lankan southern coast, the eastward SMC dominates during the southwest monsoon (yellow shading in Fig. 4) with a maximum surface transport of 13.4–21.5 Sv in June (Fig. 4b). The eastward flow is surface intensified but can extend to the deepest analyzed depth of 600 m (Fig. 3b). The PIES-altimetry and SMAP SSS show that the SMC transports saline water originating in the AS along the Sri Lankan southern coast during the southwest monsoon in agreement with findings from prior studies based on hydrographic surveys, climatological salinity, and model simulations (Vinayachandran et al. 2013, 1999; Han and McCreary 2001; Sanchez-Franks et al. 2019). However, this eastward transport of the AS water is not necessarily contiguous around the Sri Lankan eastern coast due to the presence of the SLD that arises from westward-propagating Rossby waves and Ekman pumping over the BoB (Vinayachandran et al. 1999; Wijesekera et al. 2016a; Fig. 5b).

Our PIES measurements show that the southward-flowing flank of the SLD is very strong in this season and usually extends to the deepest analyzed depth of 600 m; it transports 14–20 Sv in the upper 200 m of the water column (Fig. 4a). The occasional opposing subsurface flow is only briefly apparent at the eastern section in June of each year (Fig. 3a). As Anutaliya et al. (2017) suggested, the core of the undercurrent in June is very deep with the maximum speed typically

occurring at 900 m, and so is below the depth resolved by our observations. Satellite altimetry shows that the saline water during the southwest monsoon is often wrapped around the eastern flank of the SLD (around ~85.5°E) and thus flows northward farther from Sri Lanka (Fig. 5b). The imported saline water is sometimes recirculated southward along the eastern coast by the SLD resulting in convergence at the southeastern coast of Sri Lanka (Fig. 5b). The recirculation can also produce negative eddy salt transport along the Sri Lankan eastern coast, for example like that observed in 2015 (Fig. 6a).

2) Fall monsoon transition (September–October)

Along the Sri Lankan southern coast, the SMC often continues into the fall monsoon transition (brown shading in Fig. 4). With the exception of 2016 [when a strong negative IOD (nIOD) occurs], surface northward flow is present along the Sri Lankan eastern coast in this season, suggesting a continuous pathway of volume transport along the Sri Lankan eastern and southern coasts during these years (Figs. 3 and 4). Also, satellite altimetry patterns confirm the connection of these boundary currents at the surface during the fall monsoon transition of 2017 and 2018 similar to the monthly mean (Fig. 5c). The reconstructed velocity profile shows that the northward flow off the Sri Lankan eastern coast is not only present at the surface but can also extend over the 0–600-m-depth layer (Fig. 3a).

In 2017, the altimetry-derived circulation maps show the northward flow of the SMC at the eastern section more offshore, centered around ~83.5°E (farther offshore than presented in the monthly map; Fig. 5c). This may be the reason that the northward current through the eastern PIES section in 2017 transports much fresher water with a salinity of 33.1–33.2, as compared with that along the southern coast where the salinity is 34.6–34.8. During the fall monsoon transition of 2018, satellite measurements show a strong eastward surface current associated with the saline water from the low-latitude region (to the south of 5°N) of the central or western AS (to the west of 70°E) occurring off the southern coast. The eastward current turns sharply around the southeastern coast of Sri Lanka centered around ~82°E (closer to the coast than shown in the monthly mean map; Fig. 5c) to transport saline water into the BoB producing a positive eddy salt flux along both the southern and eastern Sri Lankan coasts (Fig. 6). Similarly, during the 2015 fall monsoon transition, the PIES at the eastern section, satellite altimetry, and satellite SSS also suggest the import of saline water into the BoB along the southern and eastern coasts of Sri Lanka. This BoB salt import around Sri Lanka originating in the western equatorial IO during the fall monsoon transition is consistent with previous numerical studies (Jensen 2001, 2003; Sanchez-Franks et al. 2019). Thus, the PIES observations highlight the role of saline water imported into the BoB via the boundary currents during the fall transition of some years.

3) Northeast monsoon (November–December)

During the northeast monsoon (blue shading in Fig. 4), the southward EICC off the Sri Lankan eastern coast observed in previous studies (Shetye et al. 1996; Wijesekera et al. 2015) is apparent for ~1–2 months between October and January (roughly the northeast monsoon season) in every year of the PIES record (Fig. 4a). The EICC is strongest near the surface and extends to the deepest observed depth of 600 m (Fig. 3a), which is comparable to that derived from a single hydrographic survey at 11°N (Shetye et al. 1996). Off the southern coast, the WMC occupies the region; thus, the flow is predominantly westward particularly in the surface layer (0–200-m depth; Figs. 3b and 4b). Southward flow along the Sri Lankan eastern coast occurs at the same time as westward flow along the southern coast every year, strongly suggesting a connection between the EICC and the WMC (Figs. 1, 3, 4, 5d). The satellite surface geostrophic velocity also confirms the westward pathway of the surface EICC around the Sri Lankan southern coast during these periods (Fig. 5d). The PIES-satellite observations provide the first observation-based estimate of simultaneous eddy salt flux showing the export of freshwater by the EICC and the WMC along the Sri Lankan eastern and southern coasts over multiple years. Although the continuous flow along the two coasts persists over only a relatively short period (1–2 months), 4×10^6–6×10^6 kg s^{-1} of eddy salt transport is present (Figs. 5d and 6).

The relatively short duration of the continuous flow along the Sri Lankan eastern and southern coasts is likely a result of a westward-propagating Rossby wave radiated from the eastern boundary of the BoB during the northwest monsoon that often affects the circulation off the Sri Lankan southeastern coast. The westward propagation of the Rossby wave from the eastern boundary of the BoB is also apparent in satellite altimetry (Sreenivas et al. 2012). The Rossby waves arriving offshore of Sri Lanka cause bifurcation of the southward EICC with one branch flowing southward or southeastward leaving a weaker westward flow along the southern coast.

The surface velocity derived from satellite altimetry indicates that the EICC and the WMC usually do not fully extend over the width of the PIES section (Fig. 5d; Wijesekera et al. 2015; Rainville et al. 2022). Thus, with only two PIES deployed at the section end-points, the true EICC width and the associated eddy salt transport may not always be accurately represented as the section may also include recirculation in the interior of the BoB. Also, the SMAP SSS product within ~50 km off the eastern coast and ~20 km off the southern coast is unavailable because the satellite-measured SSS is highly contaminated in the land–sea transition region (Grodsky et al. 2018; Fig. 5). Since the low-salinity water is often transported out of the BoB along the Sri Lankan eastern and southern coasts in a narrow alongshore current during the northeast monsoon, the calculated eddy salt transport might underrepresent the role of the EICC and the WMC in the BoB freshwater export. Thus, the estimated values should serve as a lower bound of the volume transport and actual eddy salt transport, particularly during the northeast monsoon season.

4) Spring monsoon transition (March–April)

During the spring transition (green shading in Fig. 4), the westward-flowing North Equatorial Current (NEC) is present in the southern BoB at 5°–8°N (Cutler and Swallow 1984;

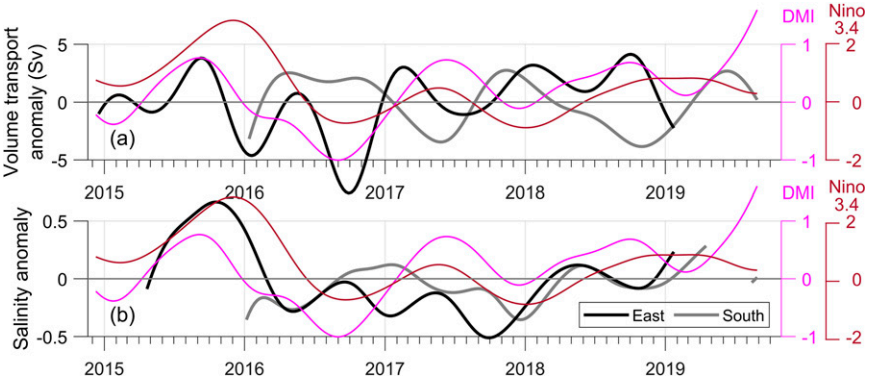

FIG. 7. (a) Volume transport anomalies (Sv) in the surface layer (0–200-m depth) along the Sri Lankan eastern (black) and southern (gray) coasts, and (b) section-mean SMAP SSS anomalies at the eastern (black) and southern (gray) coasts, with the same 120-day low-pass-filtered DMI (magenta) and Niño-3.4 index (maroon) being depicted in both panels. The anomaly values are calculated by removing the seasonal cycles and frequencies higher than 120 days.

Wijesekera et al. 2016a; Fig. 1) and bifurcates at the southeastern coast of Sri Lanka (Fig. 5a; Shetye et al. 1993; Hacker et al. 1998). The bifurcation produces the observed northward surface flow along the eastern coast (Eigenheer and Quadfasel 2000; Durand et al. 2009; Anutaliya et al. 2017) and westward flow along the Sri Lankan southern coast where the westward-flowing WMC is still present (Figs. 3, 4, 5a). The reconstructed velocity profile shows that the northward current at the eastern section is usually confined to the upper 150–250 m of the water column (Fig. 3a). Below the northward surface layer, a southward-flowing spring undercurrent is apparent along the Sri Lankan eastern coast in March and April throughout the PIES observing period, consistent with the previous study of Anutaliya et al. (2017) that is based on sporadic observations and numerical simulations. As the water being transported by the NEC originates in the southern BoB, the salinity does not deviate much from the mean salinity; thus, eddy salt transport during the spring monsoon transition is often small. Still, the northward flow along the Sri Lanka eastern coast sometimes yields weak positive eddy salt flux, e.g., in 2018 (Fig. 6).

5) SUMMARY ON SEASONAL VARIABILITY

The PIES observations highlight periods of high positive $F_s(t)$ along the eastern coast of Sri Lanka that occur not only during the northeast monsoon season, as found in previous studies (Han and McCreary 2001; Wijesekera et al. 2015), but positive $F_s(t)$ also occurs during the fall monsoon transitions in some years, e.g., 2015 and 2018 (Fig. 6). Despite the continuous eddy salt transport between the south and east sections that mainly occurs during the fall monsoon transition and the northeast monsoon, the correlation between salt fluxes along the eastern and southern coasts is only 0.34 (significant at the 95% confidence level) over the overlapping observed period (Figs. 5a and 6).

d. Year-to-year variability of the regional circulation

1) YEAR-TO-YEAR VARIABILITY OF EDDY SALT FLUX

At the eastern section, the mean eddy salt fluxes for the individual years over the observing period vary from -0.23×10^6 to 1.05×10^6 kg s^{-1} with the 2015 annual-mean eddy salt flux calculated only from April to December due to because of the limited availability of the SMAP SSS during that year (Table 2). Still, the time-mean eddy salt flux over the missing months (January–March) is usually small (Figs. 5a and 7a). The uncertainty associated with the annual-mean salt flux estimation is 0.17×10^6 kg s^{-1} (Table 1). The eddy salt flux across the southern section averaged over each individual year ranges from 0.98×10^6 to 1.51×10^6 kg s^{-1} with an uncertainty of 0.31×10^6 kg s^{-1} (Tables 1 and 2), generally higher than that at the eastern section. Note that the low value of mean annual eddy salt flux in 2019 is simply due to the observing period that ends at the beginning of November, and thus does not fully capture the seasonally high eddy salt transport during the northeast monsoon (Fig. 6b).

2) ROLE OF THE 2016 NIOD EVENT ON THE BOUNDARY CURRENTS

To examine year-to-year variability of the boundary currents and salt being transported, the low-frequency components (anomaly) of the volume transport and SSS are calculated by removing the 4-yr seasonal cycle and signals with period shorter than 120 days (Fig. 7a). The anomalies are compared with the low-frequency component of the dipole mode index (DMI) that indicates IOD activity (Saji et al. 1999) and the mean sea surface temperature in the Niño-3.4 region (Niño-3.4 index). The correlation between the transport anomaly off the eastern coast and the DMI is 0.65, suggesting an anomalous southward flow during an nIOD event, and likewise the correlation between the transport anomaly off the southern coast and the DMI is −0.52, suggesting an anomalous eastward flow during an nIOD event (Table 3); the correlation is significant at the 95% confidence level. Negative IOD events are often associated with weakening of the easterlies over the equatorial IO in August–September (Saji et al. 1999; Schott et al. 2009), which results in the development of strong downwelling Kelvin waves at the eastern boundary of the IO and around the coastal rim of the BoB, that is, equatorward flow anomaly. The Kelvin waves

TABLE 3. Correlation coefficients r between the low-frequency components of the climate mode indices [dipole mode index (label DMI) and mean sea surface temperature in the Niño-3.4 region (label Niño-3.4)] and the low-frequency components of volume transport, section-mean SSS, and eddy salt transport at the eastern and southern sections. Asterisks denote values that are not significant at the 95% confidence level.

	East		South	
	DMI	Niño-3.4	DMI	Niño-3.4
Volume transport	0.65	0.02*	−0.52	−0.38
Section-mean SSS (entire period)	0.31	0.76	0.13*	−0.06*
Section-mean SSS (July 2016 onward)	0.07*	0.32	—	—
Eddy salt transport	0.67	0.44	−0.40	−0.52

have seemingly little impact off the southern coast (Sreenivas et al. 2012). Also, the seasonal Rossby waves radiated from the eastern BoB are modified by changes in the equatorial winds during IOD events. This usually affects the circulation off the eastern coast of Sri Lanka more than that off the southern coast (Sreenivas et al. 2012). Thus, the volume transport along the Sri Lankan eastern coast is anomalously southward during negative IOD in agreement with findings from previous numerical studies (Thompson et al. 2006; Dandapat et al. 2018), while that along the southern coast exhibits little deviation from its seasonal cycle during the 2016 nIOD event (Figs. 3 and 4). As the nIOD event in 2016 reached its peak in October 2016, the anomalous southward flow along the eastern coast opposed the seasonal northward boundary current during the fall monsoon transition and obscured it.

Negative eddy salt transport along the Sri Lankan eastern coast, corresponding to BoB freshwater import or saline water export, is likely during an nIOD event as suggested by the positive correlation (Table 3). To determine how SSS at the section fluctuates during IOD events, correlation between section-mean SSS and DMI is calculated. Although the correlation between the DMI and the mean SSS off the eastern coast is positive, it is mainly dominated by the anomalously high SSS during the second half of 2015 when a weak positive IOD event and the 2015/16 El Niño simultaneously occur (Fig. 7a). The SSS deviation is in fact small and the SSS increases as the 2016 nIOD develops, hence this is not consistent with the calculated positive correlation for the entire period. Correlation between the low-frequency DMI and low-frequency SSS from July 2016 onward, when the 2015/16 El Niño no longer dominates, is near zero and is not significant at the 95% confidence level (Table 3). The evidence suggests no connection between the IOD variability and the surface salinity pattern at the eastern section even though a previous study indicates low BoB freshwater input during nIOD events (Durand et al. 2011). Therefore, the positive correlation between the low-frequency DMI and eddy salt transport at the eastern section (Table 3) is likely caused by the anomalous volume transport alone (Figs. 4a and 7). The deviation of the SSS at the eastern section does not significantly contribute to the variation of the eddy salt transport under the influence of the IOD events. Similarly, the DMI only significantly correlates with the volume transport anomaly and does not correlate with the section-mean SSS at the southern section (Fig. 7; Table 3). Thus, the significant anticorrelation there between the low-frequency eddy salt transport and the DMI is likely caused by the anomalous volume transport along the southern coast of Sri Lanka.

During the 2016 nIOD event, the anomalously southward flow along the Sri Lankan eastern coast and anomalously eastward flow along the southern coast cause an anomalous confluence of flow at the southeastern coast slightly after the event is fully developed, during the fall monsoon transition. The confluence is associated with southward flow of saline water yielding a negative eddy salt transport along the Sri Lanka eastern coast and anomalously eastward flow along the southern coast yielding a positive eddy salt transport (Figs. 3, 4, 6; Table 3). Thus, the lowest annual-mean eddy salt transport at the eastern section and highest annual-mean eddy salt transport at the southern section are found in 2016 (Table 2). However, the anomalous confluence of saline water tends to continue northeastward into the BoB at ~85.5°E. The circulation pattern is similar to that observed during the southwest monsoon of a neutral year (Fig. 5b). Thus, the overall eddy salt transport into the BoB is expected to increase during the 2016 nIOD event.

3) ROLE OF THE 2015/16 EL NIÑO EVENT ON THE BOUNDARY CURRENTS

Along the Sri Lankan eastern coast, El Niño conditions potentially strengthen the northward flow during the fall monsoon transition and weaken the southward-flowing EICC during the northeast monsoon (Pant et al. 2015) due to the suppression of seasonal downwelling Kelvin waves (Sreenivas et al. 2012). However, the eastern-section transport anomaly does not exhibit such strong deviation from the seasonal cycle during the 2015/16 El Niño (Fig. 7a). The correlation of the transport anomaly with the Niño-3.4 index is near zero and not significant at the 95% confidence level (Table 3). Off the southern coast, weak negative correlation is found between the volume transport anomaly and the low-frequency component of the Niño-3.4 index ($r = -0.38$), suggesting anomalously westward volume transport during El Niño conditions, and vice versa. A previous study based on satellite measurements found that the eastern equatorial wind is anomalously westward during an El Niño causing suppression of the seasonal downwelling Kelvin waves during the northeast monsoon (Sreenivas et al. 2012). As a result, the boundary current along the Sri Lankan southern coast is anomalously westward.

A correlation between the SSS anomaly at the Sri Lankan eastern section and the Niño-3.4 index suggests anomalously saline water during an El Niño event ($r = 0.76$; Fig. 7b; Table 3). However, interannual SSS variability in other parts of the BoB, e.g., the northeastern and central BoB, has shown to be unrelated to ENSO variability (Chaitanya et al. 2015; Pant et al. 2015). As the correlation between volume transport along the eastern coast and the Niño-3.4 index is not significant at the 95% confidence

level at low-frequency time scales, the increase in eddy salt transport along the eastern coast during an El Niño event is mainly dominated by the presence of anomalously saline water (Table 2; Fig. 7b). In contrast, the significant anticorrelation between the low-frequency components of eddy salt transport off the southern coast and Niño-3.4 index likely contributes from the presence of anomalously westward flow during an El Niño event as correlation between the Niño-3.4 and the section-mean SSS is not significant (Table 3).

The PIES observations during the 2015/16 El Niño event show the largest annual eddy salt flux along the Sri Lankan eastern coast in 2015 when highly saline water, up to 10.6×10^6 kg s^{-1} of salt originating from the AS, is transported northward by the seasonal current during the fall monsoon transition (Figs. 3a, 4a, 5c). The anomalously saline water occurs shortly before the 2015/16 El Niño is fully developed (Fig. 7b). The satellite-derived surface geostrophic current and SSS show that the northward flow of saline water along the eastern coast is a part of an anticyclonic eddy and does not effectively result in a net transport of saline water into the BoB. Off the Sri Lankan southern coast, the PIES were unfortunately not yet deployed during the 2015/16 El Niño. The altimetry-derived surface current in fall of 2015, however, does not deviate from the seasonal mean (not shown), despite the significant anticorrelation between the volume transport anomaly and the low-frequency Niño-3.4 (Table 3). Therefore, the impact of an El Niño on the BoB eddy salt transport is still unclear.

5. Summary

This study provides the first observations of high-frequency continuous volume transport and eddy salt transport measured simultaneously off both the eastern and southern coasts of Sri Lanka. The results provide a better understanding of the regional circulation as well as its contribution to the salt budget in the BoB and the variability on seasonal and interannual time scales. In addition, the PIES measurements together with the vertical structure derived from the Seaglider velocity measurements resolve the temporally varying section-mean velocity of the boundary currents providing the vertical structure of the regional currents, such as the EICC, SLD, WMC, and SMC (e.g., McCreary et al. 1996; Han and McCreary 2001; Wijesekera et al. 2015; Schott et al. 1994). High-frequency variability of the vertical structure of currents occurring during monsoon transitions, that has previously only been examined via numerical simulations (e.g., Jensen 2001; Anutaliya et al. 2017), is also revealed.

Together with the satellite SSS, the PIES measurements and satellite altimetry allows a continuous estimation of the eddy salt transport with reasonable accuracy at these sections. Glider measurements indicate that both velocity and salinity structures are more complex at the southern section and our integrated technique produces an estimated eddy salt transport that has higher uncertainty at that section. Despite this higher uncertainty, the eddy salt transports across both sections compare well to values independently computed from the Seaglider measurements while permitting a view of the higher-frequency component of the transports. The observations reveal that large sudden changes in eddy salt transport often occur, thus high-frequency and continuous monitoring of the eddy salt transport is required to achieve accurate estimates. The high-frequency observations are also valuable for obtaining a better understanding of intraseasonal events, such as those associated with rainfall events during the monsoon season. The eddy salt transports also show high seasonal and interannual variability. The interannual changes in the boundary current eddy salt flux can be as large as 12%–28% of the entire salt budget of the BoB, while the mean eddy salt flux contributes 9%–27% to the BoB salt budget. As mentioned above, this should be viewed as a lower bound.

The estimates of volume transport and eddy salt transport presented here can be further improved with additional PIES and mooring measurements. The deployment of only two end-point PIES does not always capture the lateral extent of the boundary currents as the width of the boundary current can vary within the section covered. When the boundary current is narrower than the region between the PIES, the estimated volume transport within the section length could include opposing currents resulting in an underestimation of the boundary current transport. Simulations using glider velocity measurements along each PIES section show that an addition of one or two more PIES between the two existing PIES would significantly reduce the transport uncertainty associated with the varying width of the boundary current. With an additional two PIES, the transport uncertainty would be reduced from 3.7 to 0.7 Sv. In addition, neither SMAP nor the Seaglider measures the salinity very close to the coast where a strong salinity signal is expected, particularly during the northeast monsoon. The average innermost salinity measurement taken at the eastern section by the gliders is ~50 km offshore, and the innermost measurement taken by the SMAP satellite is ~50 km offshore. Likewise, the average innermost salinity measurement taken at the southern section by the gliders is ~40 km offshore, and the innermost measurement taken by the SMAP satellite is ~20 km offshore. Additional in situ salinity measurements nearer to the coast, such as might be obtained from a simple shelf mooring, would provide the missing salinity signal and likely improve the accuracy of the eddy salt transport estimation.

Acknowledgments. This work was supported by the U.S. Office of Naval Research (ONR) as part of three ONR Departmental Research Initiatives: Air–Sea Interactions Regional Initiative (ASIRI), Northern Arabian Sea Circulation–Autonomous Research (NASCar), and Monsoon Intra-Seasonal Oscillations in Bay of Bengal (MISO-BoB) through ONR Grants N00014-14-1-0629, N00014-17-1-2655 (authors A. Anutaliya and U. Send); N00014-15-1-2189 (author J. L. McClean); N00014-16-1-2313 (author J. Sprintall); and N00014-13-1-0478, N00014-15-1-2231, and N00014-17-1-2718 (authors L. Rainville and C. Lee).

Data availability statement. PIES measurements are freely available on OceanSITES (https://dods.ndbc.noaa.gov/thredds/catalog/oceansites/DATA_GRIDDED/SLBC/catalog.html).

Data collected by Seaglider are freely available online (http://hdl.handle.net/1773/48130). Hydrographic profiles are from the National Centers for Environmental Information (Boyer et al. 2013; https://www.nodc.noaa.gov/access/index.html). Argo data were collected and made freely available by the International Argo Program and the national programs that contribute to it (http://www.argo.ucsd.edu, http://argo.jcommops.org). The Argo Program is part of the Global Ocean Observing System. This study has been conducted using altimeter data from the EU Copernicus Marine Service Information (http://marine.copernicus.eu/services-portfolio/access-to-products/?option=com_csw&view=details&product_id=SEALEVEL_GLO_PHY_L4_REP_OBSERVATIONS_008_047). SMAP salinity data are produced by Remote Sensing Systems and sponsored by the NASA Ocean Salinity Science Team and are available online (https://www.remss.com).

APPENDIX

Salinity Profile Construction

At each section, local historical hydrography was used to create two salinity lookup tables; the first table has the CTD salinity profiles arranged as a function of surface velocity, while the second table has the profiles arranged as a function of SSS. Satellite-derived surface velocity or salinity at a time and location of interest is used to determine subsurface salinity structure on the basis of the first or second lookup table, respectively. The vertical structure obtained from the lookup table is then scaled such that it passes through the SMAP SSS at the corresponding time and location and through 35.0 at 600-m depth (which is the historical mean salinity at 600-m depth at both sections). The two lookup tables provide us with two options for the section-depth salinity estimation and were used to assess the skill of this method.

To test the lookup tables for the subsurface structure of salinity at the eastern and southern sections, Seaglider salinity measurements were compared with those derived from each lookup table. In most cases, the salinity profiles derived from the two lookup tables are similar. However, the second lookup table arranged as a function of SSS generally provides results that agree better with the Seaglider salinity profiles at the eastern section. At the southern section, the first lookup table with salinity profiles sorted as a function of surface velocity generally gives profiles that agree better with Seaglider salinity profiles. Therefore, the following calculation is based on these "best" salinity lookup tables determined accordingly for each section.

REFERENCES

Anutaliya, A., and Coauthors, 2017: An undercurrent off the east coast of Sri Lanka. *Ocean Sci.*, **13**, 1035–1044, https://doi.org/10.5194/os-13-1035-2017.

——, U. Send, J. Sprintall, J. L. McClean, M. Lankhorst, and J. Koelling, 2019: Mooring and seafloor pressure end-point measurements at the southern entrance of the Solomon Sea: Subseasonal to interannual flow variability. *J. Geophys. Res. Oceans*, **124**, 5085–5104, https://doi.org/10.1029/2019JC015157.

Beal, L. M., T. K. Chereskin, H. L. Bryden, and A. Ffield, 2003: Variability of water properties, heat and salt fluxes in the Arabian Sea, between the onset and wane of the 1995 southwest monsoon. *Deep-Sea Res. II*, **50**, 2049–2075, https://doi.org/10.1016/S0967-0645(03)00045-6.

Boyer, T. P., and Coauthors, 2013: World Ocean Database 2013. NOAA Atlas NESDIS 72, 209 pp., http://doi.org/10.7289/V5NZ85MT.

Chaitanya, A. V. S., and Coauthors, 2015: Observed year-to-year sea surface salinity variability in the Bay of Bengal during the 2009–2014 period. *Ocean Dyn.*, **65**, 173–186, https://doi.org/10.1007/s10236-014-0802-x.

Cutler, A. N., and J. C. Swallow, 1984: Surface currents of the Indian Ocean (to 25°S, 100°E). IOS Tech. Rep. 187, 8 pp., https://eprints.soton.ac.uk/14603/.

D'Addezio, J. M., B. Subrahmanyam, E. S. Nyadjro, and V. S. N. Murty, 2015: Seasonal variability of salinity and salt transport in the northern Indian Ocean. *J. Phys. Oceanogr.*, **45**, 1947–1966, https://doi.org/10.1175/JPO-D-14-0210.1.

Dandapat, S., A. Chakraborty, and J. Kuttippurath, 2018: Interannual variability and characteristics of the East India Coastal Current associated with Indian Ocean Dipole events using a high resolution regional ocean model. *Ocean Dyn.*, **68**, 1321–1334, https://doi.org/10.1007/s10236-018-1201-5.

de Vos, A., C. B. Pattiaratchi, and E. M. S. Wijeratne, 2014: Surface circulation and upwelling patterns around Sri Lanka. *Biogeosciences*, **11**, 5909–5930, https://doi.org/10.5194/bg-11-5909-2014.

Ducet, N., P. Y. L. Traon, and G. Reverdin, 2000: Global high-resolution mapping of ocean circulation from TOPEX/Poseidon and ERS-1 and -2. *J. Geophys. Res.*, **105**, 19 477–19 498, https://doi.org/10.1029/2000JC900063.

Durand, F., D. Shankar, F. Birol, and S. S. C. Shenoi, 2009: Spatiotemporal structure of the East India Coastal Current from satellite altimetry. *J. Geophys. Res.*, **114**, C02013, https://doi.org/10.1029/2008JC004807.

——, F. Papa, A. Rahman, and S. K. Bala, 2011: Impact of Ganges-Brahmaputra interannual discharge variations on Bay of Bengal salinity and temperature during 1992–1999 period. *J. Earth Syst. Sci.*, **120**, 859–872, https://doi.org/10.1007/s12040-011-0118-x.

Eigenheer, A., and D. Quadfasel, 2000: Seasonal variability of the Bay of Bengal circulation inferred from TOPEX/Poseidon altimetry. *J. Geophys. Res.*, **105**, 3243–3252, https://doi.org/10.1029/1999JC900291.

Garternicht, U., and F. Schott, 1997: Heat fluxes of the Indian Ocean from a global eddy-resolving model. *J. Geophys. Res.*, **102**, 21 147–21 159, https://doi.org/10.1029/97JC01585.

Girishkumar, M. S., M. Ravichandran, M. J. McPhaden, and R. R. Rao, 2011: Intraseasonal variability in barrier layer thickness in the south central Bay of Bengal. *J. Geophys. Res.*, **116**, C03009, https://doi.org/10.1029/2010JC006657.

Grodsky, S. A., D. Vandemark, and H. Feng, 2018: Assessing coastal SMAP surface salinity accuracy and its application to monitoring Gulf of Maine circulation dynamics. *Remote Sens.*, **10**, 1232, https://doi.org/10.3390/rs10081232.

Hacker, P., E. Firing, and J. Hummon, 1998: Bay of Bengal currents during the northeast monsoon. *Geophys. Res. Lett.*, **25**, 2769–2772, https://doi.org/10.1029/98GL52115.

Han, W., and J. P. McCreary, 2001: Modelling salinity distributions in the Indian Ocean. *J. Geophys. Res.*, **106**, 859–877, https://doi.org/10.1029/2000JC000316.

Jensen, T. G., 2001: Arabian Sea and Bay of Bengal exchange of salt and tracers in an ocean model. *Geophys. Res. Lett.*, **28**, 3967–3970, https://doi.org/10.1029/2001GL013422.

——, 2003: Cross-equatorial pathways of salt and tracers from the northern Indian Ocean: Modelling results. *Deep-Sea Res. II*, **50**, 2111–2127, https://doi.org/10.1016/S0967-0645(03)00048-1.

Kennelly, M., K. Tracy, and D. R. Watts, 2007: Inverted Echo Sounder data processing manual. University of Rhode Island Graduate School of Oceanography Tech. Rep. 2007-02, 87 pp., https://digitalcommons.uri.edu/physical_oceanography_techrpts/2/.

Krishnamohan, K. S., and Coauthors, 2019: Is there an effect of Bay of Bengal salinity on the northern Indian Ocean climatological rainfall? *Deep-Sea Res. II*, **166**, 19–33, https://doi.org/10.1016/j.dsr2.2019.04.003.

Lee, C. M., and Coauthors, 2016: Collaborative observations of boundary currents, water mass variability, and monsoon response in the southern Bay of Bengal. *Oceanography*, **29**, 102–111, https://doi.org/10.5670/oceanog.2016.43.

McCreary, J. P., W. Han, D. Shankar, and S. R. Shetye, 1996: Dynamics of the East India Coastal Current 2. Numerical solutions. *J. Geophys. Res.*, **101**, 13 993–14 010, https://doi.org/10.1029/96JC00560.

Meinen, C. S., and D. R. Watts, 1998: Calibrating inverted echo sounders equipped with pressure sensors. *J. Atmos. Oceanic Technol.*, **15**, 1339–1345, https://doi.org/10.1175/1520-0426(1998)015<1339:CIESEW>2.0.CO;2.

——, and ——, 2000: Vertical structure and transport on a transect across the North Atlantic Current near 42°N: Time series and mean. *J. Geophys. Res.*, **105**, 21 869–21 891, https://doi.org/10.1029/2000JC900097.

Meissner, T., F. J. Wentz, and A. Manaster, 2018: Remote Sensing Systems SMAP ocean surface salinities [level 3 running 8-day], version 3.0 validated release. Remote Sensing Systems, accessed 7 April 2019, www.remss.com/missions/smap.

Pant, V., M. S. Girishkumar, T. V. S. Udaya Bhaskar, M. Ravichandran, F. Papa, and V. P. Thangaprakash, 2015: Observed interannual variability of near-surface salinity in the Bay of Bengal. *J. Geophys. Res. Oceans*, **120**, 3315–3329, https://doi.org/10.1002/2014JC010340.

Pirro, A., H. J. S. Fernando, H. W. Wijesekera, T. G. Jensen, L. R. Centurioni, and S. U. P. Jinadasa, 2020: Eddies and currents in the Bay of Bengal during summer monsoons. *Deep-Sea Res. II*, **172**, 104728, https://doi.org/10.1016/j.dsr2.2019.104728.

Qin, S., H. Wang, J. Zhu, L. Wang, Y. Zhang, and H. Wang, 2020: Validation and correction of sea surface salinity retrieval from SMAP. *Acta Oceanol. Sin.*, **39**, 148–158, https://doi.org/10.1007/s13131-020-1533-0.

Rainville, L, C. M. Lee, K. Arulananthan, S. U. P. Jinadasa, H. J. S. Fernando, W. N. C. Priyadarshani, and H. Wijesekera, 2022: Water mass exchanges between the Bay of Bengal and Arabian Sea from multiyear sampling with autonomous gliders. *J. Phys. Oceanogr.*, **52**, 2377–2396, https://doi.org/10.1175/JPO-D-21-0279.1.

Rao, R. R., and R. Sivakumar, 2003: Seasonal variability of sea surface salinity and salt budget of the mixed layer of the north Indian Ocean. *J. Geophys. Res.*, **108**, 3009, https://doi.org/10.1029/2001JC000907.

——, M. S. Girish Kumar, M. Ravichandran, V. V. Gopalakrishna, and P. Thadathil, 2008: A cold pool south of Indo-Sri Lanka channel and its intrusion into the southeastern Arabian Sea during winter. *Deep-Sea Res. I*, **55**, 1009–1020, https://doi.org/10.1016/j.dsr.2008.04.006.

Reppin, J., F. A. Schott, and J. Fischer, 1999: Equatorial currents and transports in the upper central Indian Ocean: Annual cycle and interannual variability. *J. Geophys. Res.*, **104**, 15 495–15 514, https://doi.org/10.1029/1999JC900093.

Saji, N. H., B. N. Goswami, P. N. Vinayachandran, and T. Yamagata, 1999: A dipole in the tropical Indian Ocean. *Nature*, **401**, 360–363, https://doi.org/10.1038/43854.

Sanchez-Franks, A., and Coauthors, 2019: The railroad switch effect of seasonally reversing currents on the Bay of Bengal high-salinity core. *Geophys. Res. Lett.*, **46**, 6005–6014, https://doi.org/10.1029/2019GL082208.

Schott, F. A., and J. P. McCreary, 2001: The monsoon circulation of the Indian Ocean. *Prog. Oceanogr.*, **51**, 1–123, https://doi.org/10.1016/S0079-6611(01)00083-0.

——, J. Reppin, and J. Fischer, 1994: Currents and transports of the Monsoon Current south of Sri Lanka. *J. Geophys. Res.*, **99**, 25 127–25 141, https://doi.org/10.1029/94JC02216.

——, S. P. Xie, and J. P. McCreary, 2009: Indian Ocean circulation and climate variability. *Rev. Geophys.*, **47**, RG1002, https://doi.org/10.1029/2007RG000245.

Sengupta, D., G. N. Bhsrath Raj, and S. S. C. Shenoi, 2006: Surface freshwater from Bay of Bengal runoff and Indonesian Throughflow in the tropical Indian Ocean. *Geophys. Res. Lett.*, **33**, L22609, https://doi.org/10.1029/2006GL027573.

Shankar, D., P. N. Vinayachandran, and A. S. Unnikrishnan, 2002: The monsoon currents in the north Indian Ocean. *Prog. Oceanogr.*, **52**, 63–120, https://doi.org/10.1016/S0079-6611(02)00024-1.

Shenoi, S. S. C., D. Shankar, and S. R. Shetye, 2002: Differences in heat budgets of the near-surface Arabian Sea and Bay of Bengal: Implications for the summer monsoon. *J. Geophys. Res.*, **107**, 3052, https://doi.org/10.1029/2000JC000679.

Shetye, S. R., A. D. Gouveia, S. S. C. Shenoi, D. Sundar, G. S. Michael, and G. Nampoothiri, 1993: The western boundary current of the seasonal subtropical gyre in the Bay of Bengal. *J. Geophys. Res.*, **98**, 945–954, https://doi.org/10.1029/92JC02070.

——, ——, D. Shankar, S. S. C. Shenoi, P. N. Vinayachandran, D. Sundar, G. S. Michael, and G. Nampoothiri, 1996: Hydrography and circulation in the western Bay of Bengal during the northeast monsoon. *J. Geophys. Res.*, **101**, 14 011–14 025, https://doi.org/10.1029/95JC03307.

Shroyer, E., and Coauthors, 2021: Bay of Bengal intraseasonal oscillations and the 2018 monsoon onset. *Bull. Amer. Meteor. Soc.*, **102**, E1936–E1951, https://doi.org/10.1175/BAMS-D-20-0113.1.

Sprintall, J., and M. Tomczak, 1992: Evidence of the barrier layer in the surface layer of the tropics. *J. Geophys. Res.*, **97**, 7305–7316, https://doi.org/10.1029/92JC00407.

Sreenivas, P., C. Gnanaseelan, and K. V. S. R. Prasad, 2012: Influence of El Niño and Indian Ocean Dipole on sea level variability in the Bay of Bengal. *Global Planet. Change*, **80–81**, 215–225, https://doi.org/10.1016/j.gloplacha.2011.11.001.

Tang, W., and Coauthors, 2017: Validating SMAP SSS with in situ measurements. *Remote Sens. Environ.*, **200**, 326–340, https://doi.org/10.1016/j.rse.2017.08.021.

Thadathil, P., P. M. Muraleedharan, R. R. Rao, Y. K. Somayajuly, G. V. Reddy, and C. Revichandran, 2007: Observed seasonal variability of barrier layer in the Bay of Bengal. *J. Geophys. Res.*, **112**, C02009, https://doi.org/10.1029/2006JC003651.

Thompson, B., C. Gnanaseelan, and P. S. Salvekar, 2006: Variability in the Indian Ocean circulation and salinity and its impact on SST anomalies during dipole events. *J. Mar. Res.*, **64**, 853–880, https://doi.org/10.1357/002224006779698350.

Vinayachandran, P. N., and T. Yamagata, 1997: Monsoon response of the sea around Sri Lanka: Generation of thermal domes and anticyclonic vortices. *J. Phys. Oceanogr.*, **28**, 1946–1960, https://doi.org/10.1175/1520-0485(1998)028<1946:MROTSA>2.0.CO;2.

——, Y. Masumoto, T. Mikawa, and T. Yamagata, 1999: Intrusion of the southwest monsoon current into the Bay of Bengal. *J. Geophys. Res.*, **104**, 11 077–11 085, https://doi.org/10.1029/1999JC900035.

——, V. S. N. Murty, and V. Ramesh Babu, 2002: Observations of barrier layer formation in the Bay of Bengal during summer monsoon. *J. Geophys. Res.*, **107**, 8018, https://doi.org/10.1029/2001JC000831.

——, D. Shankar, S. Vernekar, K. K. Sandeep, P. Amol, C. P. Neema, and A. Chatterjee, 2013: A summer monsoon pump to keep the Bay of Bengal salty. *Geophys. Res. Lett.*, **40**, 1777–1782, https://doi.org/10.1002/grl.50274.

Watts, D. R., C. Sun, and S. Rintoul, 2001: A two-dimensional gravest empirical mode determined from hydrographic observations in the Subantarctic Front. *J. Phys. Oceanogr.*, **31**, 2186–2209, https://doi.org/10.1175/1520-0485(2001)031<2186:ATDGEM>2.0.CO;2.

Weller, R. A., and Coauthors, 2016: Air-sea interaction in the Bay of Bengal. *Oceanography*, **29**, 28–37, https://doi.org/10.5670/oceanog.2016.36.

Wijesekera, H. W., and Coauthors, 2015: Southern Bay of Bengal currents and salinity intrusions during the northeast monsoon. *J. Geophys. Res. Oceans*, **120**, 6897–6913, https://doi.org/10.1002/2015JC010744.

——, W. J. Teague, D. W. Wang, E. Jarosz, and T. G. Jensen, 2016a: Low-frequency currents from deep moorings in the southern Bay of Bengal. *J. Phys. Oceanogr.*, **46**, 3209–3238, https://doi.org/10.1175/JPO-D-16-0113.1.

——, and Coauthors, 2016b: ASIRI: An ocean-atmosphere initiative for Bay of Bengal. *Bull. Amer. Meteor. Soc.*, **97**, 1859–1884, https://doi.org/10.1175/BAMS-D-14-00197.1.

Wilson, E. A., and S. C. Riser, 2016: An assessment of the seasonal salinity budget for the upper Bay of Bengal. *J. Phys. Oceanogr.*, **46**, 1361–1376, https://doi.org/10.1175/JPO-D-15-0147.1.

Xie, S. P., and S. G. H. Philander, 1994: A coupled ocean-atmosphere model of relevance to the ITCZ in the eastern Pacific. *Tellus*, **46A**, 340–350, https://doi.org/10.3402/tellusa.v46i4.15484.